Nanoscale

PAPER

View Article Online
View Journal | View Issue

Cite this: *Nanoscale*, 2024, **16**, 10262

Enabling white color tunability in complex 3D-printed composites by using lead-free self-trapped exciton 2D perovskite/carbon quantum dot inks†

Tawanwit Luangwanta, [a,b] Silver-Hamil Turren-Cruz, *[a,c] Sofia Masi, [a] Samrat Das Adhikari, [a] Ileana B. Recalde, [a] Marcileia Zanatta, [a] Diego Iglesias,[a] Jhonatan Rodríguez-Pereira, [d] Santi Gené-Marimon, [e] Eugenia Martinez-Ferrero, [e] Sulawan Kaowphong, [b] Emilio Palomares, [e,f] Victor Sans, [a] Andrés F. Gualdrón-Reyes *[a,g] and Iván Mora-Seró *[a]

The generation of stable white light emission using lead-free perovskites remains a huge challenge in the development of future display and lighting technologies, due to fast material deterioration and the decrease of the color quality. In this work, we report a combination of diverse types of 2D A_2SnX_4 (A = bulky cation, X = Br, I) perovskites exhibiting self-trapped exciton (STE) emission and blue luminescent carbon quantum dots (CQDs), with the purpose of generating A_2SnX_4/CQD inks with a broadband emission in the visible region and a tunable white light color. By varying the concentration of the 2D perovskite, the white emission of the mixtures is modulated to cool, neutral, and warm tonalities, with a PL quantum yield up to 45%. From the combinations, the PEA_2SnI_4/CQD-based ink shows the longest stability, due to suitable surface ligand passivation provided by the capping ligands covering the CQDs, compensating the defect sites in the perovskite. Then, by incorporating the PEA_2SnI_4/CQDs inks into an acrylate polymer matrix, the quenching of the PL component from the perovskite was restrained, being stable for >400 h under ambient conditions and at a relative humidity of ~50%, and allowing the preparation of complex 3D-printed composites with stable white emission tonalities. This contribution offers an application of STE-based Sn-perovskites to facilitate the future fabrication of lead-free white-light optoelectronic devices.

Received 19th February 2024,
Accepted 21st April 2024

DOI: 10.1039/d4nr00707g

rsc.li/nanoscale

1. Introduction

For several years, halide perovskites (HPs) have favored the fast development of efficient photovoltaic and optoelectronic devices due to their fascinating intrinsic properties, including good light-absorption ability, suitable electronic properties, versatile surface chemistry, and high color purity.[1–3] Therefore, these materials have been considered the most revolutionary semiconductors, reaching breakthroughs in operational efficiency in the above technologies. Recently, they have been good candidates for the fabrication of the next generation of liquid crystal display (LCD) prototypes,[4,5] being able to produce high-quality white emission, with a better color rendering index (CRI) and a wide color gamut compared to commercial phosphor-based LCDs available on the market. However, the ionic nature of the HPs, especially those with a 3D structure, makes them prone to progressive degradation under moisture[6] or photoirradiation,[7] deteriorating their structural integrity. In addition, the presence of Pb is one of the most pivotal obstacles to the commercialization of these inno-

[a]*Institute of Advanced Materials (INAM), Universitat Jaume I (UJI), Avenida de Vicent Sos Baynat, s/n, 12071 Castelló de la Plana, Castellón, Spain. E-mail: silver.turren@gmail.com, andres.gualdron@uach.cl, sero@uji.es*
[b]*Department of Chemistry, Center of Excellence in Materials Science and Technology, Faculty of Science, Chiang Mai University, Chiang Mai 50200, Thailand*
[c]*Department of Physical Chemistry, Polish Academy of Sciences, Warsaw 01-224, Poland*
[d]*Center of Materials and Nanotechnologies, Faculty of Chemical Technology, University of Pardubice, Nam. Cs. Legii 565, 53002 Pardubice, Czech Republic*
[e]*The Institute of Chemical Research of Catalonia – CERCA (ICIQ-CERCA), Tarragona, 43007, Spain*
[f]*ICREA, Passeig Lluís Companys, 28, 08010 Barcelona, Spain*
[g]*Facultad de Ciencias, Instituto de Ciencias Químicas, Universidad Austral de Chile, Isla Teja, Valdivia, 5090000, Chile*

†Electronic supplementary information (ESI) available: Experimental setup, morphology, and optical properties of CQDs, XRD patterns of the as-prepared A_2SnX_4 perovskites, PLQY measurements of A_2SnX_4/CQDs inks, PL spectra with the corresponding CIE diagrams, XPS spectra, surface chemical composition, ^1H NMR spectra and TRPL decay curves for white-light emitting PEA_2SnI_4/CQD samples. See DOI: https://doi.org/10.1039/d4nr00707g

vative materials due to the growing demand for the use of non-toxic elements and partial replacement of Pb from the HP structure.[8] Among the most prominent candidates, Sn^{2+} is a suitable metal cation to substitute Pb^{2+}, promoting the fabrication of potential lead-free Sn-HP-based devices.[9–11] Unfortunately, Sn^{2+} is easily oxidized to Sn^{4+}, generating Sn-vacancies and a high density of defects in the perovskite.[12,13] These defect sites induce the formation of carrier traps that decrease the performance of the Sn-HP devices.[14,15] Therefore, the incorporation of lead-free perovskites into the LCD technology to generate white-light emission is hindered by the fast deterioration of the structural integrity of the material, which would decrease the quality of the color, leading to low CRI values. Some alternative lead-free structures such as vacancy ordered double perovskites have been studied to generate stable white light through the appearance of a single broadband emission, where the color quality can be modulated as a function of the chemical composition.[16,17] However, this feature would not allow the facile emergence of white color tonalities, which is a practical drawback, for instance, in image processing applications where an adequate color balance needs to be achieved.

Therefore, the study of A_2SnX_4 structures (A = bulky alkylammonium cations, X = Br, I) has been highlighted to overcome the limitations in the use of Sn-HPs, attending to the fact that the organic species are located on the perovskite surface to give stability against moisture and water.[18–20] In a typical 2D structure, bulky organic cations are beyond the tolerance limit, acting as spacers between the inorganic $[SnX_6]^{4-}$ octahedral layers. This feature defines the optical, electronic, and carrier mobility properties of the 2D HPs.[21,22] Although composition engineering can modify the band gap of the photomaterial (by varying the type of halide), the intercalation of the organic spacers with diverse geometries or organic functional moieties through the stacking layers can also favor the octahedral distortion,[23] which is another way to control the photophysical properties. Interestingly, some A_2SnX_4 perovskites exhibit two kinds of emission features: (i) band-to-band (b–b) PL,[24,25] where the electrons accumulated in the conduction band (CB) can recombine with photogenerated holes in the valence band (VB), making the absorption edge and PL spectrum with narrow full width at half maximum (FWHM) get close together (small Stokes shifted PL), and (ii) a broadband emission (wide FWHM) which emerges in the visible region even though the absorption edge of the 2D HPs is within the UV range. This is a characteristic of the formation of non-accessible located states in the wide bandgap of the perovskite, where photons are emitted with a lower energy than the band gap (large Stokes shifted PL). This phenomenon is called self-trapped exciton (STE),[25–27] which has been used to prepare promising materials for solid-state lighting. Under this concept, the synthesis of alkylammonium tin bromide (OLA_2SnBr_4) microplates with a high PL quantum yield (PLQY) of ~88% and the fabrication of orange-emitting LEDs with external quantum efficiencies of ~0.1% have been reported.[28] Other potential applications include the fabrication of luminescent solar concentrators, where the STE-based perovskites can absorb UV light to emit photons in the visible range, minimizing the self-absorption and providing transparency,[29] adequate for solar windows. However, most applications involving 2D Sn-HPs require materials with optical features based on b–b transitions, ideal for charge transport and light emission, taking advantage of the fast emission from the band-edge carrier radiative relaxation.

Nevertheless, the appearance of a broadband emission from STE-based Sn-HPs would allow them to cover a wide range of the yellow-orange-red region from the energy spectrum, making them suitable candidates for the generation of white light emission in combination with other light-emitting nanomaterials. In a previous study, we used carbon quantum dots (CQDs) as suitable materials to combine with Pb-HPs (red-emitting $CsPbI_3$), providing a broadband emission in the visible spectrum and favoring the generation of high-quality white color tonalities (cool-white, CW; neutral white, NW; and warm white, WW).[30] In this work, we have combined STE-based A_2SnX_4 microcrystals with blue-emitting CQDs to obtain inks with modifiable white color emission. The variation of the Sn-HP content in the mixture allowed us to achieve CW, NW, and WW tonalities with a PLQY of up to 45%. Interestingly, by varying the separation distance between the $[SnX_6]^{4-}$ layers composing the Sn-HPs, depending on the A-site cation, the modification of the emission mechanism can occur as well due to a dynamic interaction between the perovskite organic cation and the CQD organic shell.[31] This premise can describe the fast or delayed deterioration of the white color quality in the prepared mixtures. After adding the A_2SnX_4/CQDs inks to an acrylate polymer matrix, composites were stable for >400 h under ambient conditions, at a relative humidity (RH) of ~50%, allowing the fabrication of 3D-printed white light-emitting solids with complex shapes. These findings open the door to the utilization of STE-based 2D Sn-perovskites as a step forward to produce scalable lead-free white-light optoelectronic devices with desirable color tunability and quality.

2. Results and discussion

The nature of the organic spacer and halides influences the photophysical features of the perovskite samples. For this reason, two different 2D A_2SnX_4 perovskites through the colloidal hot-injection have been synthesized by modifying a procedure reported elsewhere.[28] Using oleylammonium (OLA^+) and phenethylammonium (PEA^+) as A-site cations and bromine and iodine as the X halides, the following perovskite systems are obtained: OLA_2SnBr_4, OLA_2SnI_4 and PEA_2SnI_4. To obtain information about the morphology of the as-prepared perovskites, transmission electron microscopy (TEM) images were recorded (Fig. 1A–C). We observed a microplate-type shape in OLA_2SnX_4, with diameters of 4.1 ± 1.7 μm (OLA_2SnI_4) and 6.5 ± 2.5 μm (OLA_2SnBr_4), while PEA_2SnI_4 exhibited a microsheet-type form with a size of 4.9 ± 2.0 μm. The corres-

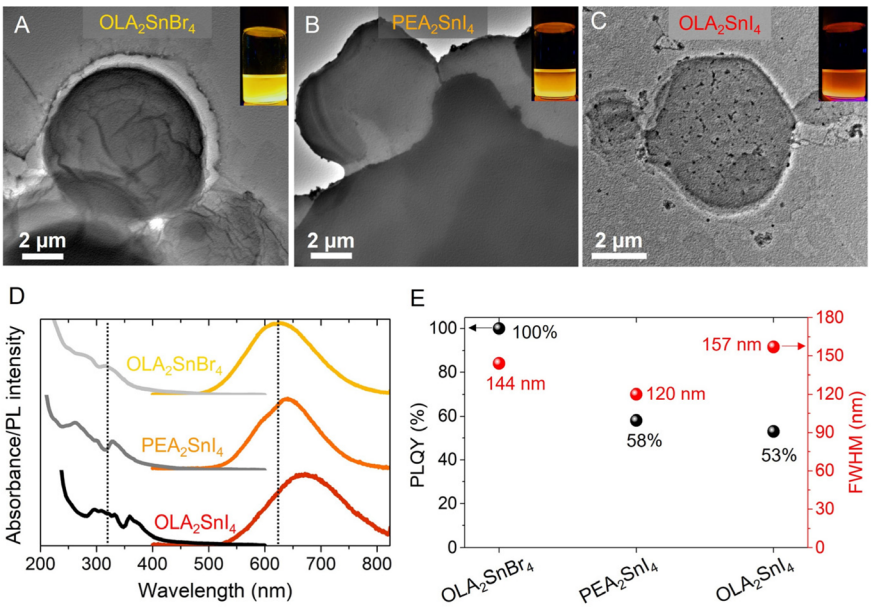

Fig. 1 TEM images of the as-prepared (A) OLA_2SnBr_4, (B) PEA_2SnI_4, and (C) OLA_2SnI_4. (D) Typical absorption/PL spectra and (E) PLQY and PL FWHM of the corresponding A_2SnX_4 perovskite microcrystals. The insets of Fig. 1A–C show the STE-based emission of the 2D perovskites under 365 nm-UV illumination.

ponding particle size distribution is shown in Fig. S1.† Then, as seen in the insets of Fig. 1A–C, the corresponding as-prepared perovskite dispersions generate a yellow-orange-red emission under UV irradiation. By measuring the optical properties of these materials (Fig. 1D), we evidenced the absorption edge/PL peak position at 316/620 nm, 330/640 nm, and 357/671 nm for OLA_2SnBr_4, PEA_2SnI_4, and OLA_2SnI_4, respectively, confirming the appearance of the intrinsic STE phenomenon as the main radiative recombination pathway for the 2D Sn-perovskites.[25,28] This PL feature is maintained for 15 days under ambient air before the quenching starts (Fig. S2†). Additionally, the nature of the organic spacer and halides influences the perovskite samples' photophysical features. The substitution of Br by I in OLA_2SnX_4 produces a redshift in the absorption edge and the PL peak position of the perovskite, narrowing its band gap.[32] Due to the fact that halide substitution generates mainly a variation of electronic states coming from the VB (due to the replacement of Br 4p by I 5p orbitals),[33] the VBM is closer to the STE energy levels, which would explain the displacement of the broadband emission to higher wavelengths. Furthermore, OLA_2SnBr_4 achieved a PLQY of 100%, while OLA_2SnI_4 exhibited a PLQY of 53% (Fig. 1E). This change is attributed to the emergence of defect sites in the $[SnI_6]^{4-}$ octahedra,[27] considering that the iodide species show a higher lability than that of Br ones to diffuse out from the perovskite.[33]

On the other hand, substituting the OLA^+ cation with PEA^+ to prepare the PEA_2SnI_4 perovskite induces a slight blueshift of the Abs/PL emission features, distinguishing two different contributions in the PL spectrum. Even though OLA^+ is a larger cation than PEA^+, this aromatic cation has been reported to produce high octahedral distortion in $[MX_6]^{4-}$ units, for instance, in the $[PbI_6]^{4-}$ layers from PEA_2PbI_4, when the length of the equatorial Pb–I bonds is elongated.[23] This fact extends the atomic overlapping between the metal and I orbitals, increasing the energy separation between the VB and the CB.[34] The distortion of the inorganic Sn–I layers in the presence of PEA^+ can explain the emergence of the two PL signals associated with isolated $[SnI_6]^{4-}$ units (shorter wavelengths) and the interconnection of octahedra through the crystal edge (longer wavelengths).[18] Then, PEA_2SnI_4 showed a PLQY of 58%, quite similar to that of OLA_2SnI_4. Lastly, the FWHM values of the 2D perovskites were determined to be 144, 157, and 120 nm for OLA_2SnBr_4, OLA_2SnI_4, and PEA_2SnI_4, respectively (Fig. 1E). This feature is very useful to cover a wide range of the yellow-orange-red region of the energy spectrum (Fig. 1D), mediating the generation of a broadband emission in all the visible region, in combination with luminescent CQDs, to produce white light (see below). From the XRD patterns of OLA_2SnX_4 and PEA_2SnI_4 perovskites, provided in Fig. S3 of the ESI,† a periodicity in the XRD peaks can be observed. This is the typical feature of a layered 2D perovskite structure (n = 1). By calculating the d-spacing through their corresponding periodicity values,[21] we evidenced that the separation between the inorganic octahedral layers from OLA_2SnI_4 is smaller (2.8 nm) than that of OLA_2SnBr_4 (4.4 nm), ascribed to (i) the bigger size of $[SnI_6]^{4-}$ than $[SnBr_6]^{4-}$ units and (ii) the appearance of an A-site deficiency in the iodide perovskite. For PEA_2SnI_4, a d-spacing of 1.8 nm was achieved, larger than the reported value for red-emitting PEA_2SnI_4.[35] We associate this discrepancy to some modifications in the intramolecular packing of the PEA^+ cations from the 2D structure of the perovskite, which generates the octahedral distortion. The fact that OLA^+ species induces a higher $[SnX_6]^{4-}$ separation than

PEA^+ would give the possibility to an accelerated deterioration of the structural integrity of the OLA_2SnX_4 perovskites, which could explain the presence of cracks and black dots in their surface (Fig. 1A and C) and the fast quenching of the STE-PL intensity, compared to PEA_2SnI_4 (Fig. S2†).

After studying the photophysical properties of the as-synthesized A_2SnX_4 perovskites, we proceeded to add different contents of these materials to a fixed concentration of the CQD colloidal solution (6 mg mL^{-1} in hexane), achieving the corresponding mixtures with perovskite concentrations varying from 1.4 to 2.1 mg mL^{-1}. The morphology and optical properties of the CQDs are shown in Fig. S4 in the ESI†. Fig. 2A–C exhibits the PL spectra of the A_2SnX_4/CQDs inks (λ_{exc} = 350 nm), for which two main PL signals were achieved. A broad PL emission associated with the CQDs was centered at 480 nm, showing a redshift compared to the PL feature obtained for the solution of carbon nanoparticles. Meanwhile, the broadband emissions attributed to the presence of OLA_2SnBr_4 and OLA_2SnI_4 are located at ~597 and 668 nm, respectively, presenting a slight blueshift in comparison with the PL emission of the pure perovskites. The variation of the optical features for CQDs and Sn-HPs before and after the combination indicates their dynamic interaction in the prepared mixtures. The displacement of the STE-based broadband emission to smaller wavelengths could result from octahedral distortion in the OLA_2SnX_4 systems,[23] by the loss of labile OLA^+ cations. In the case of PEA_2SnI_4, the negligible shift of the PL emission indicates the presence of more stable structural integrity in the perovskite during the preparation of mixtures.

Then, the increase in the perovskite content generates a higher STE-PL intensity in all the mixtures, allowing the modulation of the white-light emission in the CW, NW, and WW tonalities, as is evidenced in the Commission Internationale de l'Eclairage (CIE) color space (Fig. 2A′–C′) and the corresponding color temperature obtained from CIE coordinates (Fig. S5A, ESI†). However, the PL intensity of CQDs is slightly/strongly quenched depending on the nature of the perovskites. After adding the lowest content of the A_2SnX_4 microcrystals to the mixture (1.4 mg mL^{-1}), we noted that the PL emission of CQDs decreases in the following order: OLA_2SnI_4/CQDs > PEA_2SnI_4/CQDs > OLA_2SnBr_4 (Fig. 2A–C). This trend agrees with the separation between the PL peak positions of CQDs and Sn-HPs, which the OLA_2SnI_4/CQD system depicts as the largest. In this scenario, we suggest the charge transfer from energy levels contained from CQDs (from larger wavelengths) to the perovskite after photon absorption,[30] which mediates the decrease of PL in CQDs and favors the STE mechanism in the 2D perovskites. This process tends to increase the PLQY in the OLA_2SnX_4/CQD inks, independently of the bare CQD PL (Fig. S5B, ESI†). Surprisingly, for the PEA_2SnI_4/CQD system, the PLQY value is almost similar even when more perovskite was added to the ink, deducing that a different interaction between CQDs and PEA_2SnI_4 was occurring in the mixture. At

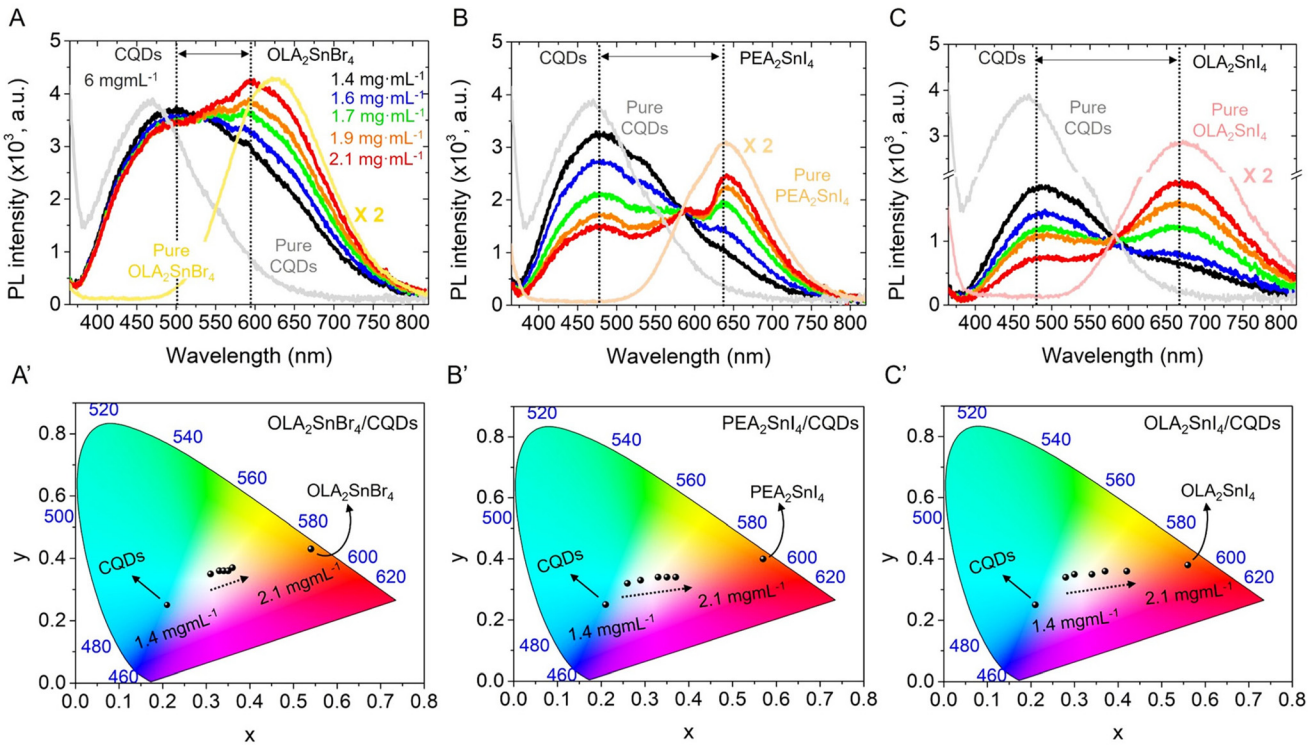

Fig. 2 (A–C) PL spectra and their corresponding (A′–C′) CIE diagrams of the prepared white-light emitting (A and A′) OLA_2SnBr_4/CQDs, (B and B′) PEA_2SnI_4/CQDs and (C and C′) OLA_2SnI_4/CQD mixtures by varying the perovskite content (1.4–2.1 mg mL^{-1}) in the 6 mg mL^{-1} CQDs solution. PL emission of pure CQDs and A_2SnX_4 is also shown for comparative purposes.

this point, we can conclude that white light emission coordinates obtained from the combination between CQDs and A_2SnX_4 can be controlled, suggesting that the charge transfer towards the perovskite improves the STE pathway. This fact preserves or increases the white color quality of the ink.

To provide a wide analysis of the stability of the different A_2SnX_4/CQDs inks, we measured the PL properties of the corresponding mixtures with the NW light emission as a function of time (after 7 h) under ambient air and RH ~ 50%. We have chosen this color tonality as both the PL peaks for the CQDs and Sn-HP components show a similar initial intensity. As seen in Fig. 3A and C, the PL intensity of OLA_2SnX_4 rapidly quenches after 3 h under exposure to the environment. Taking into account that OLA^+ cations exhibit a weak binding capability to the perovskite structure[36] and also produce a significant separation between the inorganic $[SnX_6]^{4-}$ octahedral layers (observed from the XRD results), we suggest that the 2D structure can eventually deteriorate, promoting the loss of the STE feature in the material. Simultaneously, the PL emission intensity of the CQDs also decreased in the presence of these OLA_2SnX_4 perovskites (Fig. S6A and C, ESI†), influencing the PLQY of the samples after 7 h. For OLA_2SnBr_4/CQDs and OLA_2SnI_4/CQD systems, the PLQY values decreased from 39 and 22%, respectively, to ~6% (Fig. S6D, ESI†). Considering that the pure CQDs show a stable PLQY of ~33% after 7 h, the PL of the above mixtures is quenched due to defect states from the Sn-HPs, and the CIE color did not reach the respective feature of the pure carbon nanoparticles (Fig. 3A′ and C′). This means that the optical performance of the CQDs has been modified by a weakened degree of the ligand interaction with the perovskite system (organic shell affects the carrier recombination mechanism in the CQDs and passivates or not possible in-gap states on the surface of the emitting core).[31,37] We hypothesize a direct interaction between OLA_2SnX_4 perovskites and the hexadecylamine (HDA)/citric acid (CA) shell covering the CQD surface, considering the redshift observed for the PL component of the carbon nanoparticles (Fig. 3A and C). Interestingly, for PEA_2SnI_4/CQDs, the STE-PL quenching and the shift in the CIE tonality are delayed (Fig. 3B and B′), observing a gradual improvement of the PL contribution from CQDs (Fig. S6B, ESI†) and a higher PLQY than that of the OLA_2SnX_4/CQD mixtures over time (Fig. S6D, ESI†). This is an indication of better stability of this type of perovskite–CQD combination for a long time. Thus, HDA and CA and PEA^+ can favor the stabilization/passivation of the PEA_2SnI_4–CQD system, maintaining the STE features for a longer time.

In this scenario, it has been reported that the PL mechanism of CQDs is mainly dominated by the surface states with different energy levels (some of them closer to the ground state from CQDs), provided by surface functional groups such as –COOH and $–NH_2$, to lead the electron radiative relaxation.[38,39] In this context, the higher the density of surface oxygenated groups in the CQDs, the higher the density of surface states contained in the nanoparticles to capture excitons.[39] The presence of these states favors the electron transfer from the carbon core, where direct radiative recombination

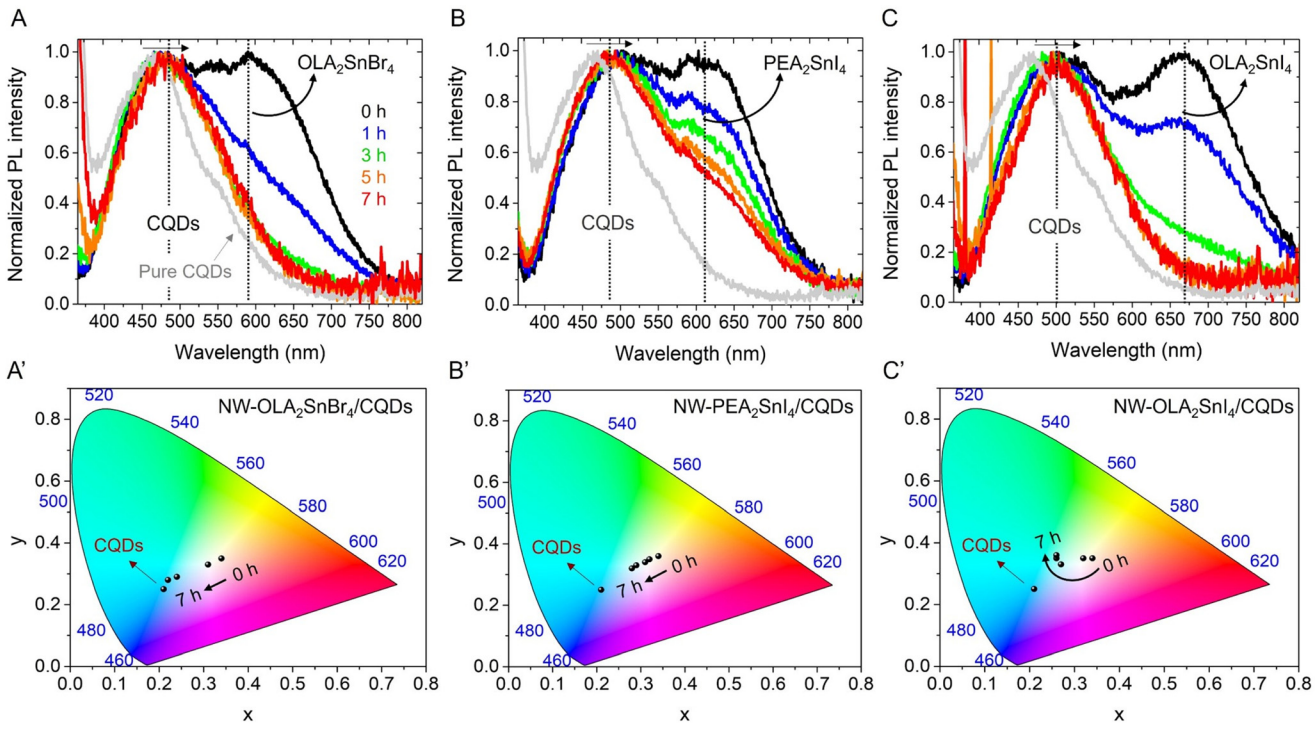

Fig. 3 (A–C) Normalized PL spectra and their corresponding (A′–C′) chromaticity diagrams of the prepared NW-emitting (A and A′) OLA_2SnBr_4/CQDs, (B and B′) PEA_2SnI_4/CQDs and (C and C′) OLA_2SnI_4/CQD mixtures by varying the aging time. The perovskite content was 1.7 mg mL^{-1} in the 6 mg mL^{-1} CQDs solution.

occurs. In the case of a high density of surface NH_2 groups, lone pairs in N atoms can fill surface states and reduce their energy separation (emergence of continuous energy levels), causing the energy gap to narrow between the VB and the CB of CQDs.[37,38] Accordingly, in addition to both of the possibilities for the carrier recombination in CQDs under a high density of (i) –COOH and (ii) $–NH_2$, (our CQDs contain HDA and CA on the surface), a charge transfer process could be promoted from CQDs to STE levels from the A_2SnX_4 perovskites to increase their PL properties (Scheme S1, ESI†). Therefore, we infer that the lowering and redshift of the PL contribution from the CQDs in the presence of OLA_2SnX_4 would lead to a decrease in the density of surface –COOH and $–NH_2$ functionalities in the CQDs–OLA_2SnX_4 interaction, reducing the content of surface states and electron density from N atoms for charge transfer. Conversely, the eventual increase of the PL emission of CQDs in the presence of PEA_2SnI_4 over time would indicate that the radiative relaxation into CQDs is gradually facilitated by the deterioration of the PL properties in the perovskite, without affecting widely the CQD surface.

With the purpose of obtaining valuable information on the interaction between CQDs and the PEA_2SnI_4 perovskite, we recorded the PL spectra of the PEA_2SnI_4/CQDs inks showing CW, NW, and WW light emission for 48 h under air and RH ≈ 50% (Fig. S7A–C, ESI†). Similar to the result shown in Fig. 3B, the PL contribution of the Sn-HPs was progressively decreased in all the mixtures, while the PL contribution of the CQDs eventually increased. A CW tonality with a different CIE color from the one generated by pure CQDs was obtained in the inks (Fig. S7A′–C′†), with a higher PLQY along the time (Fig. S5D, ESI†). Independent of the perovskite content added to the mixture, the PL emission of the CQDs improves, deducing that PEA_2SnI_4 does not alter largely the CQD surface. Then, through time-resolved PL (TRPL) measurements, we analyze the carrier recombination dynamics of the PEA_2SnI_4/CQD inks by varying the aging time. For this analysis, we have chosen the WW-light emitting ink as a representative sample; see Fig. S8, ESI.† A biexponential equation y fitted all the TRPL curves obtained in the function of aging time $y = y_0 + A_1 e^{-\frac{x}{\tau_1}} + A_2 e^{-\frac{x}{\tau_2}}$, to determine the corresponding PL lifetimes, τ_{avg}[30] (Table S1, ESI†). The sample was irradiated with a 405 nm pulsed laser, fixing the PL emission of the CQDs at 480 nm. In this way, we only guarantee the abs/emission process of the CQDs. Typically, for pure CQDs, τ_1 and τ_2 are associated with the direct radiative recombination at the CQD surface and the carrier recombination from the CQD core to the surface, respectively.[40,41] However, considering the CQD–perovskite interaction, we have assigned τ_2 to the charge transfer from the carbon nanoparticles to PEA_2SnI_4. Accordingly, the longer the aging time, the higher the τ_1, with a higher weight of the first component (A_1). This behavior indicates that the carrier recombination in the CQD surface is progressively favored once the STE emission of the perovskite microcrystals decreases over time, which can explain the increase of the PL emission and PLQY from CQDs (Fig. S7, ESI†).

To understand the surface chemical environment and composition of the PEA_2SnI_4/CQDs inks, we carried out X-ray photoelectron spectroscopy (XPS). In all the mixtures and pure PEA_2SnI_4 microcrystals, we identified the co-existence of C, O, N, Sn, and I; see XPS survey spectra in Fig. S9, ESI.† The surface chemistry of CQDs was also analyzed for comparative purposes. The corresponding speciation of each sample is shown in Table S2, ESI.† Fig. 4A shows the high-resolution (HR) XPS Sn 3d spectra of the PEA_2SnI_4/CQD inks with different white light tonalities and the individual perovskite, where a doublet centered at 487/496 eV was observed. These signals are ascribed to the presence of Sn^{2+} from the $[SnI_6]^{4-}$ octahedra composing the 2D perovskite.[42] On the other hand, two kinds of contributions are observed from the HR XPS I 3d spectra of the pure PEA_2SnI_4 and PEA_2SnI_4/CQDs samples, as exhibited in Fig. 4B. The first I 3d doublet at 618/630 eV is associated with the iodide species from the inorganic octahedral units, forming Sn–I bonds, while the couple centered at 620/631 eV is attributed to the existence of molecular iodine (I_2).[42] The appearance of this species indicates that a part of the iodide fraction is released from the inorganic layers, generating halide vacancies in the perovskite. Then, according to Table S2,† the I_2 fraction (described as the $(I_2/Sn + I_2)$ ratio) is lower for the inks than that of the pure PEA_2SnI_4 perovskite, deducing that the presence of CQDs is pivotal to keeping the structural integrity of the Sn-HPs. By comparing the PEA_2SnI_4/CQD mixtures, the NW light-emitting one shows the lowest I_2 fraction, suggesting this combination as the scenario where CQDs promote a suitable protective effect to prevent the formation of iodide vacancies. In contrast, the WW-light-emitting ink exhibits a higher I_2 fraction than the NW light-emitting one, inferring that more iodide was available to diffuse out from the perovskite structure and produce defect sites.

Fig. 4C shows the HR XPS O 1s spectra of PEA_2SnI_4, CQD, and the PEA_2SnI_4/CQD inks, with some critical differences. While pure PEA_2SnI_4 depicts two contributions at 531 and 532 eV, ascribed to the formation of (C═O)–N or Sn–O (these signals can be overlapped) and C═O bonds, respectively,[43] CQDs exhibit the co-existence of C═O and COOH moieties, at 532 and 533 eV,[44,45] respectively. In the case of CQDs, the obtained signals are attributed to the presence of a carboxyl functional group (R-COOH) provided by CA, used to synthesize the nanoparticles. Then, the contributions of C═O and COOH bonds were also detected for all the inks, with the appearance of a new signal ~530 eV corresponding to the Sn–O bond[46] and without the (C═O)–N interaction. Lastly, we revealed the typical XPS N 1s spectra for PEA_2SnI_4, CQDs and the inks (Fig. 4D), detailing two prominent peaks for the pure perovskite located at 401 and 403 eV. Taking into account the XPS N 1s assignations for another type of alkylammonium species, for instance, octylammonium cations,[25] these peaks can be associated with (C═O)–N and C–NH_3^+ species, coming from the PEA^+ cations composing the 2D perovskite. Nevertheless, only a single peak for the CQDs and the PEA_2SnI_4/CQD mixtures was noted centered at ~400 eV, attributed to C–NH_2 from the hexadecylamine (HDA) ligand covering the carbon nanoparticles.[47] The co-exist-

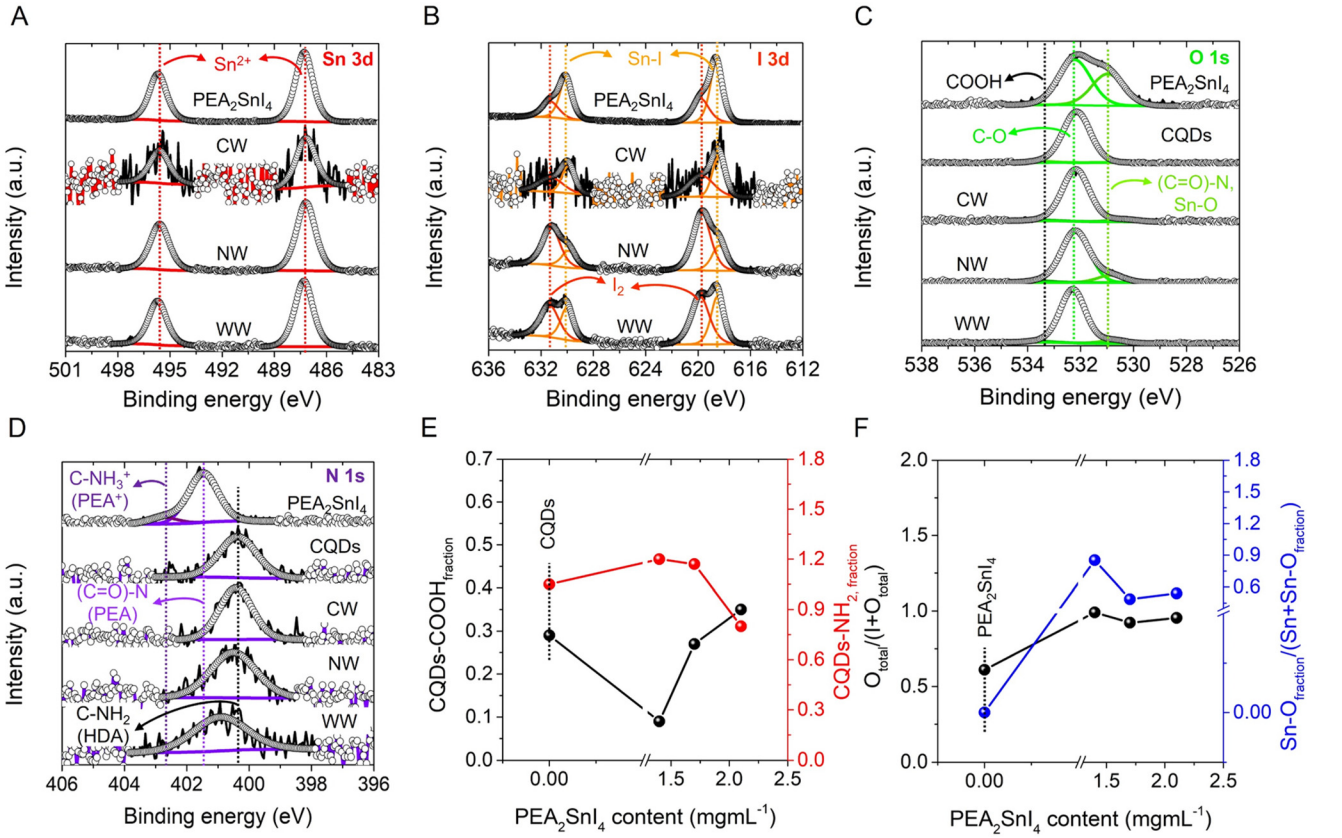

Fig. 4 High-resolution XPS (A) Sn 3d, (B) I 3d, and (C) O 1s and (D) N 1s spectra for the CW-, NW-, and WW-light emitting PEA_2SnI_4/CQD mixtures. XPS analysis was also conducted for pure PEA_2SnI_4 and CQDs for comparative purposes. (E) Estimated total COOH and NH_2 fractions from CQDs and (F) calculated total oxygen-to-halide/total Sn–O-to-Sn ratios of the PEA_2SnI_4/CQD system by varying the perovskite content in the mixture.

ence of (C═O)–N, C═O and NH_3^+ species in the pure perovskite indicates the generation of phenethylammonium oleate (PLM). As we have reported previously, by using high temperatures to prepare perovskites through colloidal synthesis in the presence of an amine and a carboxylic acid, the corresponding alkylammonium carboxylate species is formed, being the primary ligand to stabilize the final product.[48] Then, from the ^{1}H NMR spectra recorded for the pure PEA_2SnI_4 and the PEA_2SnI_4/CQD mixtures (Fig. S10, ESI†), a triplet at $\delta \sim 2.08$ ppm was observed, associated with CH_2– near the COOH functionality from free OA.[36,49] Additionally, a signal is observed at a similar chemical shift for pure CQDs, attributed to the presence of CH_2– coming from the R-COOH moiety provided by CA. Simultaneously, the signals at $\delta \sim 3.01$ ppm and 1.55 ppm are assigned to CH_2– and the proton bonded to NH_2 from phenethylamine (PEA), respectively. The co-existence of OA and PEA reinforces the hypothesis about the formation of PLM during the perovskite synthesis (see explanation below).

Having described the chemical environment of the samples and according to Table S2,† it is notable that adding PEA_2SnI_4 significantly decreases the –COOH content in the CQDs. However, once the perovskite content is higher in the mixture, the –COOH content is increased, and simultaneously, the C–NH_2 content is decreased; see Fig. 4E. The formation of phenethylammonium oleate can be promoted through an acid–base reaction between PEA and OA as given in eqn (1):

$$C_8H_9NH_2 + C_{17}H_{33}COOH \rightleftharpoons C_8H_9NH_3^+ + C_{17}H_{33}COO^-. \quad (1)$$

We propose that carboxyl ligands covering the CQDs can react with PEA species to favor the generation of carboxylate anions ($R\text{-}COO^-$) and the formation of PEA^+, see eqn (2). This can elucidate the marked decrease in the initial COOH fraction in the presence of the lowest perovskite content. However, a higher free OA fraction would also be achieved, explaining the eventual increase in the –COOH content in the mixtures even higher than that of the individual CQDs. This –COOH species could be responsible for promoting the progressive increase in the PL emission of CQDs after the delayed deterioration of PEA_2SnI_4.

$$C_8H_9NH_2 + CQDs\text{–}COOH \rightleftharpoons C_8H_9NH_3^+ + CQDs\text{–}COO^-. \quad (2)$$

Simultaneously, some OA fractions can react with HDA ligands to induce the formation of HDA^+ species, see eqn (3), which are available to fill/replace some A-site cations from the 2D perovskite:

$$CQDs\text{–}C_{16}H_{33}NH_2 + C_{17}H_{33}COOH \rightleftharpoons CQDs\text{–}C_{16}H_{33}NH_3^+ + C_{17}H_{33}COO^-. \quad (3)$$

In this way, R-COO$^-$ anions from CQDs promote the formation of Sn–O bonds, mediating the compensation of halide deficiency. Through relative contents seen in Table S2,† the CW light emitting ink shows the highest Sn–O fraction (denoted as the Sn–O/Sn + Sn–O ratio) and the highest O_{total}/(O_{total} + I_{total}) ratio(Fig. 4F), indicating that a high density of defect sites in the perovskite is fully compensated. However, by increasing the perovskite content to produce the NW light emitting ink, both the Sn–O fraction and the O_{total}/(O_{total} + I_{total}) ratio are decreased, deducing that the perovskite material depicts a less defective structure. According to the fact that the higher the perovskite content, the higher the OA fraction, we infer that more HDA ligands coming from the CQDs are transformed to HDA$^+$ through the reaction in eqn (3) to fill/replace the A-site cations in the Sn-perovskite. Lastly, by adding an excess of Sn-perovskite to obtain the WW light emitting ink, it is possible to generate a slight increase in the halide defects, considering that more iodide species are available to be released as I_2, with this deficiency being passivated by the R-COO$^-$ anions. At this point, we conclude that the combination of CQDs and PEA_2SnI_4 favors the formation of R-COO$^-$ and HDA$^+$ species in the carbon nanoparticles, with the NW light emitting ink being the suitable scenario where the suppression of halide defect sites is maximized. Nevertheless, this deduction is not enough to explain how the defect passivation is conducted between the CQDs and the 2D perovskite.

Taking into account the particle size of CQDs (3.4 ± 0.7 nm, estimated by TEM), this is a bigger nanoparticle in comparison to the separation between the $[SnI_6]^{4-}$ layers from PEA_2SnI_4 (1.8 nm, obtained from XRD). Therefore, we conclude that CQDs can promote the surface passivation of defect sites in the PEA_2SnI_4 perovskite, providing a low fraction of –COOH and –NH_2 moieties without significantly compromising their PL properties. This deduction can also explain the interaction between the OLA_2SnX_4 systems and CQDs. Considering that the *d*-spacings for OLA_2SnBr_4 and OLA_2SnI_4 systems are 4.4 and 2.8 nm, respectively (Fig. S3†), these values are larger than the size of CQDs, with the integration of CQDs between the OLA_2SnX_4 inorganic layers being plausible. This fact leads to the deterioration of the 2D structure and PL quenching of CQDs. Therefore, we conclude that the PEA_2SnI_4 surface is covered by CQDs, protecting the structural integrity for a longer time. At this point, we deduce that the nature of the A-site cation is the most important parameter that affects the stability of the ink, mediating the internal interaction between the 2D structure and CQDs or externally through passivation of surface defects in the perovskite.

Once the explanation about the effect of CQDs on the defect passivation of Sn-HPs was provided, we analyzed the possibility of combining the CW, NW and WW light-emitting PEA_2SnI_4/CQDs inks with a polymeric matrix and prepared 3D printed solid composites with geometrical complex shapes and films. To this end, we introduced the luminescent inks into a mixture of acrylate monomers such as butylacrylate (BA) and isobornyl acrylate (IBA) (using 15 mol% BA and 85 mol% IBA), using 1,4-butanediol diacrylate and diphenyl(2,4,6-trimethylbenzoyl)phosphine oxide as the crosslinker agent and the UV-initiator, respectively. This allowed suitable plasticiza-

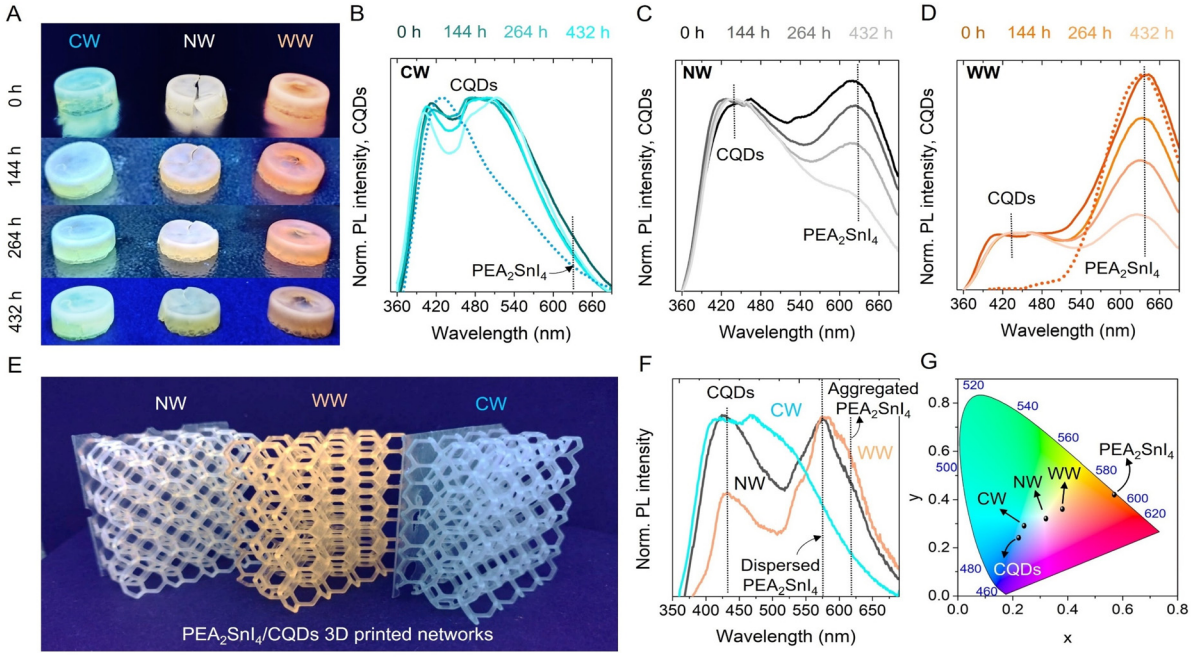

Fig. 5 (A) Photographs and the corresponding PL spectra of (B) CW-, (C) NW-, and (D) WW-light emitting PEA_2SnI_4/CQDs based-acrylate 3D composites by varying the aging time under ambient air and HR ~ 50%. (E) Photograph, (F) PL spectra and the respective (G) CIE diagram of 3D printed networks fabricated from white light emitting PEA_2SnI_4/CQDs inks. The dimensions of 3D printed networks (length × width × height) were 4 × 4 × 2 cm.

tion of the final polymeric composite, as we have reported previously for other kinds of luminescent perovskite-based 3D solids.[36] As seen in Fig. S11,† both pure CQDs and PEA_2SnI_4 were embedded into the acrylate matrix, producing the corresponding blue- and orange-emitting 3D solids. In this context, with the aim to study the changes in the PL intensity coming from the mixture between CQDs and the different contents of Sn-perovskite in the polymeric matrix, the PL properties of the PEA_2SnI_4/CQD acrylate composites in the form of pellets were obtained over time (Fig. 5A). In this way, the PLQY values of the CW-, NW- and WW-emitting PEA_2SnI_4/CQDs pellets were estimated to be 6%, 10% and 8%, respectively.

Unlike the previous discussion of the inks, where the PL emission associated with the STE properties of the perovskite is quenched after 48 h, the presence of the acrylate matrix extends the appearance of the STE emission up to 436 h under ambient air and HR ≈ 50%. This fact causes a slower modification in the PL feature, see Fig. 5B–D, and the CIE color of each ink, see Fig. S12A–C, ESI.† Although CQDs can delay the progressive deterioration of the STE emission by passivating defects in the structure of PEA_2SnI_4, the Sn^{2+}-to-Sn^{4+} oxidation cannot be totally avoided. Accordingly, the acrylate-based polymer protects the perovskite structure against oxygen and moisture,[50] hindering the fast metal oxidation and favoring the preservation of the white color emission. Interestingly, the CW-light emitting ink in both inks and composite systems shows the most stable color tonality, deducing that at the lowest perovskite content, CQDs can efficiently protect their integrity and intrinsic properties, as we observed the highest Sn–O fraction in this material through the XPS. Then, NW and WW-light emitting inks show a lower iodide defect content, achieving a decrease in the Sn–O fraction, but it is more likely to facilitate the I_2 release (being a pivotal reason to quench the PL of the perovskite). Lastly, it is possible to prepare more complex and well-defined luminescent 3D-printed shapes, as is the case of small and big polymeric networks; see Fig. S13, ESI† and Fig. 5E. Here, the prepared emissive inks are homogeneously distributed along the entire 3D composite to provide the three white-light tonalities (Fig. 5F and G), hindering the agglomeration of the perovskite. In conclusion, the combination of CQDs and Sn-HPs, such as PEA_2SnI_4, can mediate the preparation of PEA_2SnI_4/CQD mixtures, ideal for preparing suitable inks for the fabrication of luminescent 3D printed polymeric composites with tunable white-light emission.

3. Conclusions

In this work, we have shown the combination of different kinds of Sn-HP microcrystals with CQD colloidal solutions to generate a series of white-light emitting inks with modifiable color tonality. By studying the nature of the A-site cation in the A_2SnX_4/CQDs inks, we observed that the Sn-HPs based on OLA_2SnX_4 exhibit a fast quenching of their PL emission, deteriorating the white light color stability. Taking into account the weak binding capability of OLA^+ and the large separation between the inorganic $[SnX_6]^{4-}$ layers provided by this ligand, CQDs are prone to access and interact with the internal octahedral units coming from the OLA_2SnX_4 perovskites, through a high density of surface functional groups such as –COOH and $–NH_2$. This promotes the loss of structural integrity and STE features in the perovskite and PL quenching of CQDs. In contrast, Sn-HPs with smaller *d*-spacing such as PEA_2SnI_4 depict a more stable white-light emission, helping a low fraction of –COOH and $–NH_2$ moieties covering CQDs mediate the surface passivation of the perovskite. In this way, the structure and STE properties are maintained for a longer time, without altering the PL properties of CQDs. On comparison of the prepared PEA_2SnI_4/CQD inks, the NW-light emitting one is found to exhibit the lowest halide defect content in the perovskite, carrying out an efficient ligand passivation process. By increasing the PEA_2SnI_4 microcrystal content to obtain the WW light-emitting ink, the iodide fraction is increased, being more likely to favor the I_2 release and the deterioration of the STE features in the perovskite. Interestingly, although the highest defect site content is shown in the CW-light emitting ink, this combination provides the most stable white color tonality, associated with a full compensation of halide vacancies through the formation of Sn–O bonds from $R\text{-}COO^-$ moieties covering the CQDs. To preserve the intrinsic properties of the inks, an acrylate based polymeric matrix is pivotal, preventing the Sn oxidation by ligand detachment and facilitating the fabrication of white color luminescent 3D-printed composites with complex shapes. Therefore, we highlight an interesting strategy for the processability of lead-free perovskites with STE emission, being prominent for promoting the fabrication of scalable white light emitting devices.

Author contributions

A. F. G.-R. and S.-H. T.-C. designed the experiments. T. L. and A. F. G.-R. synthesized and characterized the A_2SnX_4 perovskites and CQDs. S. G.-M., E. M.-F. and E. P. synthesized and characterized the CQDs. S.-H. T.-C., S. M. and S. D. A. contributed to the analysis of materials characterization. J. R.-P. contributed to the XPS measurements and analysis. M. Z. designed and performed the NMR analysis. V. S. coordinated the experiments with polymeric matrices. I. R. formulated and stabilized the polymeric composite, prepared the 3D composite structures and performed the corresponding characterization studies of all the composites. I. R. and D. I. fabricated the PNC-composites. D. I. designed the 3D structures and optimized the printing parameters. S.-H. T.-C., A. F. G.-R. and I. M.-S. conceived the idea and oversaw the project. All authors contributed to writing the manuscript and the discussions.

Conflicts of interest

There are no conflicts to declare.

Acknowledgements

This work was supported by the Ministry of Science and Innovation of Spain (MCIN/AEI/10.13039/501100011033/), the FEDER "Una manera de hacer Europa" under Projects She-LED (PID2021-122960OA-I00), Step-Up (TED2021-131600B-C31), project ELECTROVOLT (PID2022-139866NB-I00) and by Generalitat Valenciana *via* the PROMETEO project Q-Solutions (CIPROM/2021/078). We thank the European Union's Horizon 2020 research and the Ministry of Education, Youth and Sports of the Czech Republic for the financial support of XPS measurements using the CEMNAT infrastructure (projects LM2018103 and LM2023037). S.-H. T. C. would like to thank the Spanish Ministry of Economy, Industry and Competitiveness (postdoctoral contract Juan de la Cierva Formación FJC2019-041835-I) and The National Science Centre-POLONES BIS 1 (DEC-2021/43/P/ST5/01780) for the financial support during this work. S. M. acknowledges financial support from MICINN (Spain) through the program Juan de la Cierva-Incorporatión (IJC2020-042618-I). M. Z. acknowledges the financial support from the innovation programme under the Marie Skłodowska-Curie Individual Fellowships (GA no. 101026335). V. S. thanks Generalitat Valenciana (CIDEGENT 2018/036) and UJI (B-2020-44) for funding. T. L. and S. K. thank the Institute for the Promotion of Teaching Science and Technology (IPST) and Chiang Mai University. A. F. G.-R. acknowledges to ANID through the FONDECYT Iniciación Project (Grant no. 11240161). The authors are very grateful to the "Serveis Centrals d'Instrumentació Científica (SCIC)" of the Universitat Jaume I.

References

1 J. S. Kim, J.-M. Heo, G.-S. Park, S.-J. Woo, C. Cho, H. J. Yun, D.-H. Kim, J. Park, S.-C. Lee, S.-H. Park, E. Yoon, N. C. Greenham and T.-W. Lee, *Nature*, 2022, **611**, 688–694.

2 J. Park, J. Kim, H.-S. Yun, M. J. Paik, E. Noh, H. J. Mun, M. G. Kim, T. J. Shin and S. I. Seok, *Nature*, 2023, **616**, 724–730.

3 A. Dey, J. Ye, A. De, E. Debroye, S. K. Ha, E. Bladt, A. S. Kshirsagar, Z. Wang, J. Yin, Y. Wang, L. N. Quan, F. Yan, M. Gao, X. Li, J. Shamsi, T. Debnath, M. Cao, M. A. Scheel, S. Kumar, J. A. Steele, M. Gerhard, L. Chouhan, K. Xu, X.-g. Wu, Y. Li, Y. Zhang, A. Dutta, C. Han, I. Vincon, A. L. Rogach, A. Nag, A. Samanta, B. A. Korgel, C.-J. Shih, D. R. Gamelin, D. H. Son, H. Zeng, H. Zhong, H. Sun, H. V. Demir, I. G. Scheblykin, I. Mora-Seró, J. K. Stolarczyk, J. Z. Zhang, J. Feldmann, J. Hofkens, J. M. Luther, J. Pérez-Prieto, L. Li, L. Manna, M. I. Bodnarchuk, M. V. Kovalenko, M. B. J. Roeffaers, N. Pradhan, O. F. Mohammed, O. M. Bakr, P. Yang, P. Müller-Buschbaum, P. V. Kamat, Q. Bao, Q. Zhang, R. Krahne, R. E. Galian, S. D. Stranks, S. Bals, V. Biju, W. A. Tisdale, Y. Yan, R. L. Z. Hoye and L. Polavarapu, *ACS Nano*, 2021, **15**, 10775–10981.

4 Z. Liu, L. Sinatra, M. Lutfullin, Y. P. Ivanov, G. Divitini, L. De Trizio and L. Manna, *Adv. Energy Mater.*, 2022, **12**, 2201948.

5 Q. Pan, J. Fu, S. Liu, J. Zhou, B. Ma, S. Chen, Y. Qiu, Y. Lin, Y. Hu, D. Yang, J. Chen, M.-K. Fung, Y. Wang, Q. Zhang, L. Wang and M. Cao, *Cell Rep. Phys. Sci.*, 2023, **4**, 101275.

6 Z. Zheng, L. Liu, F. Yi and J. Zhao, *J. Lumin.*, 2019, **216**, 116722.

7 R. An, F. Zhang, X. Zou, Y. Tang, M. Liang, I. Oshchapovskyy, Y. Liu, A. Honarfar, Y. Zhong, C. Li, H. Geng, J. Chen, S. E. Canton, T. Pullerits and K. Zheng, *ACS Appl. Mater. Interfaces*, 2018, **10**, 39222–39227.

8 F. Gao, X. Zhu, Q. Feng, W. Zhong, W. Liu, H. Xu and Y. Liu, *Nano Energy*, 2022, **98**, 107270.

9 Y. Wang, R. Zou, J. Chang, Z. Fu, Y. Cao, L. Zhang, Y. Wei, D. Kong, W. Zou, K. Wen, N. Fan, N. Wang, W. Huang and J. Wang, *J. Phys. Chem. Lett.*, 2019, **10**, 453–459.

10 F. Yuan, X. Zheng, A. Johnston, Y.-K. Wang, C. Zhou, Y. Dong, B. Chen, H. Chen, J. Z. Fan, G. Sharma, P. Li, Y. Gao, O. Voznyy, H.-T. Kung, Z.-H. Lu, O. M. Bakr and E. H. Sargent, *Sci. Adv.*, 2020, **6**, eabb0253.

11 J. Sanchez-Diaz, R. S. Sánchez, S. Masi, M. Krecmarová, A. O. Alvarez, E. M. Barea, J. Rodriguez-Romero, V. S. Chirvony, J. F. Sánchez-Royo, J. P. Martinez-Pastor and I. Mora-Seró, *Joule*, 2022, **6**, 861–883.

12 T. Mahmoudi, W.-Y. Rho, M. Kohan, Y. H. Im, S. Mathur and Y.-B. Hahn, *Nano Energy*, 2021, **90**, 106495.

13 H. Cao, Z. Zhang, M. Zhang, A. Gu, H. Yu, H. Ban, Q. Sun, Y. Shen, X. L. Zhang, J. Zhu and M. Wang, *Mater. Today Phys.*, 2021, **21**, 100513.

14 Z. Zhang, Y. Huang, J. Jin, Y. Jiang, Y. Xu, J. Zhu and D. Zhao, *Angew. Chem., Int. Ed.*, 2023, **62**, e202308093.

15 P. Li, X. Cao, J. Li, B. Jiao, X. Hou, F. Hao, Z. Ning, Z. Bian, J. Xi, L. Ding, Z. Wu and H. Dong, *Nano-Micro Lett.*, 2023, **15**, 167.

16 C. Chen, J. Xiang, Y. Chen, M. Jin, J. Zheng, N. Zhang and C. Guo, *Ceram. Int.*, 2022, **48**, 1851–1856.

17 F. Zhang, Z. Chen, Z. Liu, M. Jia, X. Chen, D. Wu, X. Li and Z. Shi, *J. Lumin.*, 2022, **251**, 119150.

18 V. V. Nawale, T. Sheikh and A. Nag, *J. Phys. Chem. C*, 2020, **124**, 21129–21136.

19 E. Jokar, P.-Y. Cheng, C.-Y. Lin, S. Narra, S. Shahbazi and E. Wei-Guang Diau, *ACS Energy Lett.*, 2021, **6**, 485–492.

20 C. Gao, Z. Hu, C. Yang, H. Xu, Y. Wang, J. Zhang and Y. Zhu, *Org. Electron.*, 2019, **74**, 126–134.

21 M. C. Weidman, M. Seitz, S. D. Stranks and W. A. Tisdale, *ACS Nano*, 2016, **10**, 7830–7839.

22 T. Zhang, Q. Sun, X. Zhang, Y. Shen and M. Wang, *APL Mater.*, 2021, **9**, 020906.

23 E. Mahal, S. C. Mandal and B. Pathak, *Mater. Adv.*, 2022, **3**, 2464–2474.

24 S. Li, J. Luo, J. Liu and J. Tang, *J. Phys. Chem. Lett.*, 2019, **10**, 1999–2007.

25 S. Ghimire, K. Oldenburg, S. Bartling, R. Lesyuk and C. Klinke, *ACS Energy Lett.*, 2022, **7**, 975–983.

26 Y. Han, X. Cheng and B.-B. Cui, *Mater. Adv.*, 2023, **4**, 355–373.
27 Y. Chen, Z. Wang, Y. Wei, Y. Liu and M. Hong, *Angew. Chem., Int. Ed.*, 2023, **62**, e2023016.
28 X. Zhang, C. Wang, Y. Zhang, X. Zhang, S. Wang, M. Lu, H. Cui, S. V. Kershaw, W. W. Yu and A. L. Rogach, *ACS Energy Lett.*, 2018, **4**, 242–248.
29 L. Zdražil, S. Kalytchuk, M. Langer, R. Ahmad, J. Pospíšil, O. Zmeškal, M. Altomare, A. Osvet, R. Zbořil, P. Schmuki, C. J. Brabec, M. Otyepka and Š. Kment, *ACS Appl. Energy Mater.*, 2021, **4**, 6445–6453.
30 R. R. Rad, A. F. Gualdrón-Reyes, S. Masi, B. A. Ganji, N. Taghavinia, S. Gené-Marimon, E. Palomares and I. Mora-Seró, *Adv. Opt. Mater.*, 2020, **9**, 2001508.
31 S. Tao, C. Zhou, C. Kang, S. Zhu, T. Feng, S.-T. Zhang, Z. Ding, C. Zheng, C. Xia and B. Yang, *Light: Sci. Appl.*, 2022, **11**, 56.
32 L. Lanzetta, J. M. Marin-Beloqui, I. Sanchez-Molina, D. Ding and S. A. Haque, *ACS Energy Lett.*, 2017, **2**, 1662–1668.
33 A. F. Gualdrón-Reyes, J. Rodríguez-Pereira, E. Amado-González, J. Rueda-P, R. Ospina, S. Masi, S. J. Yoon, J. Tirado, F. Jaramillo, S. Agouram, V. Muñoz-Sanjosé, S. Giménez and I. Mora-Seró, *ACS Appl. Mater. Interfaces*, 2020, **12**, 914–924.
34 M. Javed, A. Noureddine and M. Benkraouda, *Mater. Sci. Semicond. Process.*, 2023, **162**, 107490.
35 Z. Wang, F. Wang, B. Zhao, S. Qu, T. Hayat, A. Alsaedi, L. Sui, K. Yuan, J. Zhang, Z. Wei and Z. a. Tan, *J. Phys. Chem. Lett.*, 2020, **11**, 1120–1127.
36 I. Recalde, A. F. Gualdrón-Reyes, C. Echeverría-Arrondo, A. Villanueva-Antolí, J. Simancas, J. Rodriguez-Pereira, M. Zanatta, I. Mora-Seró and V. Sans, *Adv. Funct. Mater.*, 2023, **33**, 2210802.
37 X. Li, S. Zhang, S. A. Kulinich, Y. Liu and H. Zeng, *Sci. Rep.*, 2014, **4**, 4976.
38 F. Yan, Z. Sun, H. Zhang, X. Sun, Y. Jiang and Z. Bai, *Microchim. Acta*, 2019, **186**, 583.
39 H. Ding, S.-B. Yu, J.-S. Wei and H.-M. Xiong, *ACS Nano*, 2015, **10**, 484–491.
40 V. Nguyen, J. Si, L. Yan and X. Hou, *Carbon*, 2015, **95**, 659–663.
41 S. Paulo-Mirasol, S. Gené-Marimon, E. Martínez-Ferrero and E. Palomares, *ACS Appl. Electron. Mater.*, 2020, **2**, 1388–1394.
42 Y. J. Heo, H. J. Jang, J. H. Lee, S. B. Jo, S. Kim, D. H. Ho, S. J. Kwon, K. Kim, I. Jeon, J. M. Myoung, J. Y. Lee, J. W. Lee and J. H. Cho, *Adv. Funct. Mater.*, 2021, **31**, 2106974.
43 P. G. Rouxhet and M. J. Genet, *Surf. Interface Anal.*, 2011, **43**, 1453–1470.
44 D. Stefanakis, A. Philippidis, L. Sygellou, G. Filippidis, D. Ghanotakis and D. Anglos, *J. Nanopart. Res.*, 2014, **16**, 2646.
45 M. Vedamalai, A. P. Periasamy, C.-W. Wang, Y.-T. Tseng, L.-C. Ho, C.-C. Shih and H.-T. Chang, *Nanoscale*, 2014, **6**, 13119–13125.
46 H. B. Lee, N. Kumar, M. M. Ovhal, Y. J. Kim, Y. M. Song and J. W. Kang, *Adv. Funct. Mater.*, 2020, **30**, 2001559.
47 Z. Liang, B. Wang, M. Luo and H. Lu, *Diamond Relat. Mater.*, 2021, **112**, 108238.
48 E. Hassanabadi, M. Latifi, A. F. Gualdrón-Reyes, S. Masi, S. J. Yoon, M. Poyatos, B. Julián-López and I. Mora-Seró, *Nanoscale*, 2020, **12**, 14194–14203.
49 R. Grisorio, M. E. Di Clemente, E. Fanizza, I. Allegretta, D. Altamura, M. Striccoli, R. Terzano, C. Giannini, M. Irimia-Vladu and G. P. Suranna, *Nanoscale*, 2019, **11**, 986–999.
50 A. Pan, Y. Zhou, C. Zhao, C. Shi, Y. Wu, Y. Zhang, Y. Liu and L. He, *Chem. Eng. J.*, 2022, **433**, 133590.